ACS NANO

www.acsnano.org

ARTICLE

Mesoporous Polyimide Thin Films as Dendrite-Suppressing Separators for Lithium–Metal Batteries

Dong Guo, Linqin Mu, Feng Lin, and Guoliang Liu*

Cite This: *ACS Nano* 2024, 18, 155–163

Read Online

ACCESS | Metrics & More | Article Recommendations | Supporting Information

ABSTRACT: **Lithium–metal batteries require the effective suppression of lithium dendrites to guarantee both high performance and safety. Today's separators have macropores allowing lithium dendrites to traverse, leading to internal short circuits and other catastrophic results. Herein, we report a mesoporous polyimide separator for dendrite suppression. The polyimide separator exhibits mesopores of 21 nm width and a high storage modulus of 1.80 GPa. This mesoporous polyimide separator assists in the electrodeposition to form flat-top protrusions instead of sharp dendrites, therefore, allowing the safe cycling of lithium–metal batteries. This work is expected to advance the development of dendrite-suppressing strategies and contribute to the revival of lithium–metal batteries.**

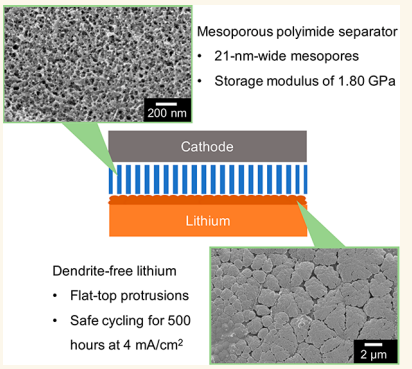

KEYWORDS: *polyimide, block copolymer, phase separation, separator, mesopore, dendrite suppression, battery*

INTRODUCTION

Lithium–metal batteries represent a high-performance energy storage technology because metallic lithium provides a high theoretical capacity of 3860 mAh/g, a low density of 0.534 g/cm^3, and a low electrochemical potential of −3.040 V vs SHE (the standard hydrogen electrode).[1−6] Since their debut in the 1970s, the commercialization of lithium–metal batteries has been plagued by severe safety concerns.[3,5] Lithium dendrites arise from the nonuniform nucleation of lithium on the anode surface.[7−9] The amplified electrical field near the lithium crystals promotes dendritic growth.[8,10] The resulting lithium dendrites expose large reactive surfaces and consume the electrolyte to form a solid-electrolyte interphase (SEI).[2,8,11,12] The uneven stripping/plating of lithium causes accumulative stress and brittle fractures in the SEI, further drying the electrolyte to grow more SEI.[2,11,13,14] This uncontrollable process deteriorates the performance of lithium–metal batteries, including increasing the internal impedance, forming isolated lithium, and lowering the Coulombic efficiency (CE).[2,8,11,12] And worse, the growing dendrites traverse the separator, causing short circuits and even fire hazards.[6,7,10] Therefore, suppressing lithium dendrites is imperative to guarantee the safe operation of high-performance lithium–metal batteries.

In the past decades, various strategies have been evaluated to suppress lithium dendrites, including (1) employing high-modulus solid-state electrolytes or ceramic-coated separators to block the dendritic growth,[15−19] (2) applying concentrated liquid electrolytes or pulse charging currents to mitigate the depletion of Li^+ near the anode surface,[2,20−22] (3) increasing operation temperatures to facilitate Li^+ diffusion,[4,23] (4) employing three-dimensional lithium–metal electrodes or hosts to enlarge the surface area,[9,24,25] and (5) engineering the composition, density, and elasticity of SEI to ensure interphase stability.[2,25−28] Although the high-modulus solid-state electrolytes are promising to suppress the dendritic growth, lithium dendrites can still penetrate the grain boundaries of the electrolytes.[16,29−31] Moreover, at room temperature, the solid-state electrolytes usually have limited conductivity and high electrolyte/electrode contact resistance.[16,29−31] Contrarily, liquid electrolytes provide high ionic conductivity and good contact with electrodes, but the dendritic growth is uncontrolled. Significantly, the deposition-diffusion competition causes Li^+ depletion near the metallic lithium surface, promoting the fast tip-growth of

Received: May 9, 2023
Revised: December 11, 2023
Accepted: December 14, 2023
Published: December 21, 2023

https://doi.org/10.1021/acsnano.3c04159
ACS Nano 2024, 18, 155–163

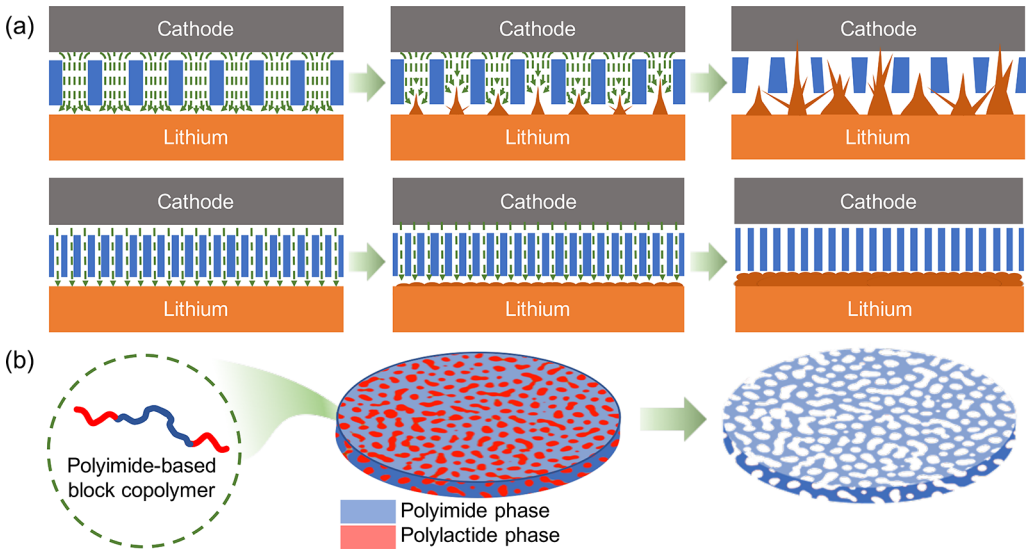

Figure 1. Effects of pore size and modulus of separators on dendrite suppression. (a) Upper: conventional macroporous PP/PE/PP separator induces nonuniform Li^+ flux and promotes uneven lithium deposition and dendritic growth. The macropores (40−400 nm wide) and low modulus of PP/PE/PP separators (~0.5 GPa in the transverse direction) cannot suppress lithium dendrites, resulting in short circuits.[33,59,60] Lower: the mesoporous polyimide separator provides uniform Li^+ flux and ensures more even lithium deposition. The mesopores and high modulus (1.80 GPa) suppress the invasion of dendrites for safe cycling. The tortuous macro/mesopores are simplified as straight pores, in which the green dashed lines represent the Li^+ flux. (b) Our strategy to prepare mesoporous, high-modulus polyimide separators from a polyimide-based block copolymer. The solution casting and chemical imidization of PLA-*b*-PAA-*b*-PLA form a polyimide-based thin film. The subsequent thermolysis produces a mesoporous polyimide separator for the lithium−metal battery.

dendrites. High-concentration liquid electrolytes, pulse charging, elevated temperatures, and high-surface-area electrodes mitigate the depletion of Li^+ near the metallic lithium surface. Still, they cannot cease the invasion of the lithium dendrites. Although the stable SEI tailors the lithium deposition, the limited mechanical strength is still vulnerable to dendritic penetration.[12,32] At the frontline of dendritic invasion, high-modulus separators are promising for suppressing unhealthy dendrite growth in liquid electrolytes.

The state-of-the-art separators are made of macroporous polyolefins such as polyethylene (PE) and polypropylene (PP). The large macropores are susceptible to lithium dendrite penetration, causing safety concerns.[33] We hypothesize that mesopores smaller than the width of lithium dendrites can provide a strong physical barrier and stop lithium dendrites from penetrating the separator. But the mesoporous separators must possess a high modulus to withstand the cumulative axial stress.[1] Compared with PE and PP, polyimides have superior mechanical performance, but controlling the pore size in polyimides on the mesoscale remains challenging. Polyimide-based separators have been produced via porogens,[22,34] phase inversion,[35−37] electrospinning,[38−42] and thermolysis of polyimide-based block copolymers.[43,44] The porogens with predefined sizes were embedded in the polyimide films and then selectively removed to template pores, i.e., silica nanospheres etched by hydrofluoric acid.[22,34] The macroscale porogens produce macropores as wide as hundreds of nanometers.[22,34] Similarly, in the phase inversion process, the nonsolvent forms macro-scale domains in the wet polyimide film, thus producing macropores as wide as hundreds of nanometers to micrometers.[35,36] The electrospinning produces a polyimide fiber mat with porosity up to 95%,[42] and the spacious interfiber voids result in micrometer-scale pores.[38−42] Different from those aforementioned strategies, the microphase separation of polyimide-based block copolymer forms mesoscale domains of tens of nanometers, holding promise for preparing mesoporous polyimides.[43,44] We adopted the strategy to prepare porous polyimides using ABA triblock copolymers comprising polyimide and thermally labile blocks. To synthesize polyimide-based triblock copolymers, various thermally labile blocks have been deployed, such as poly(methyl methacrylate),[43] polystyrene,[45,46] poly(α-methylstyrene),[47,48] polycaprolactone,[49−52] poly(ethylene oxide),[53] and poly(propylene oxide).[54−58] The triblock copolymers microphase-separate to form domains in tens of nanometers. Via thermolysis, the labile blocks decompose to create mesopores. But high-temperature thermolysis inevitably results in too-fast decomposition of the labile block, producing a large number of gaseous species, e.g., poly(α-methylstyrene) fully decomposes within 4.5 h at 325 °C.[47] The gaseous species expands in the softened polyimide matrices, resulting in pore sizes of hundreds of nanometers or even micrometers.[45] Thus, judicious selection of the labile block to achieve a low thermolysis temperature is crucial for preparing mesoporous polyimides without perturbing the porous network.

In this work, we report the preparation of a mesoporous polyimide thin film via the thermolysis of polylactide-*b*-polyimide-*b*-polylactide triblock copolymers at a low temperature of 280 °C. The thermolysis slowly removes polylactide blocks to create mesoporous polyimide thin films with a median pore width of 21 nm and a storage modulus of 1.80 GPa. The mesoporous polyimide thin films, serving as separators in lithium−metal batteries, not only show good rate capabilities comparable with PP/PE/PP trilayer separators but also assist in lithium deposition as flat-top protrusions, enabling safe long-term cycling.

RESULTS AND DISCUSSION

The mesoporous polyimide separators suppress Li dendrites following three mechanisms: (i) the mesopores uniformly

https://doi.org/10.1021/acsnano.3c04159
ACS Nano 2024, 18, 155−163

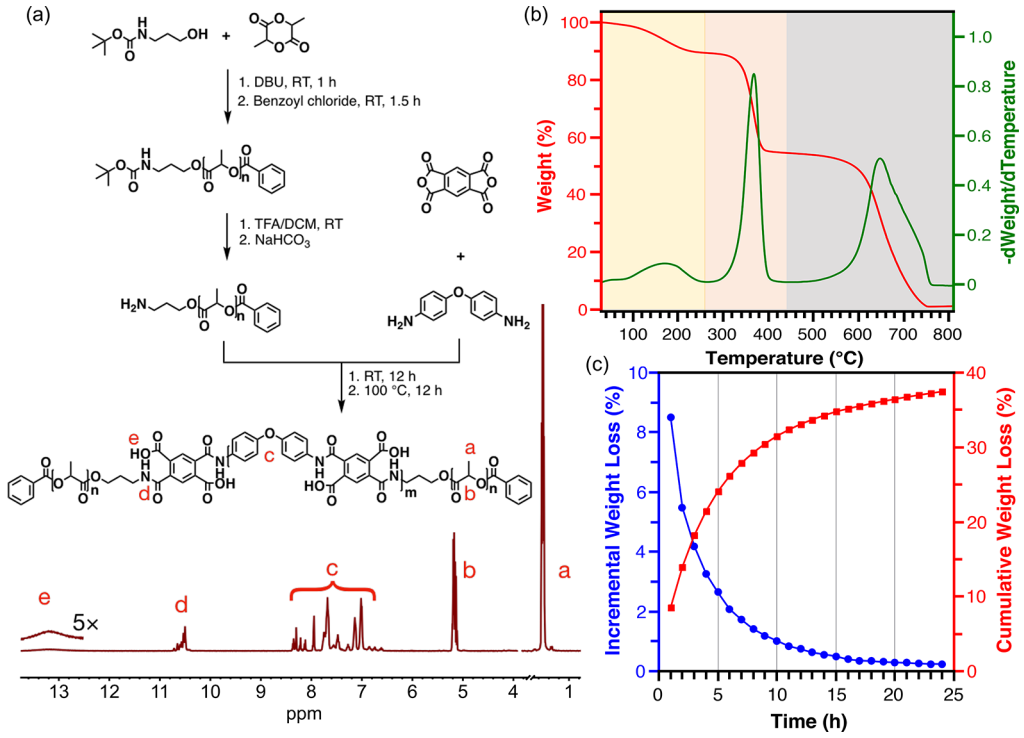

Figure 2. Synthesis and thermogravimetric analysis of PLA-*b*-PI-*b*-PLA. (a) Synthesis of PLA-*b*-PAA-*b*-PLA, and its ^{1}H NMR spectrum indicates a ϕ_{PLA} of 40.2%. (b) Thermogravimetric analysis of PLA-*b*-PI-*b*-PLA films indicates a ϕ_{PLA} of 39.0% and suggests a thermolysis temperature of PLA at 280 °C. (c) Isothermal weight loss at 280 °C for 24 h indicates the removal of most PLA.

redistribute Li^+ flux to the lithium−metal electrode, facilitating the even plating of lithium;[61,62] (ii) the mesopores are smaller than the typical width of lithium dendrites, therefore efficiently blocking the dendrites; (iii) the high modulus ceases the invasion of lithium dendrites (Figure 1a).[1,63−66] To fulfill those characteristics, on the one hand, we select polyimide as the matrix because it has high mechanical strength and a high degradation temperature. On the other hand, we select polylactide (PLA) as the sacrificial block owing to its reasonable thermolysis temperature that does not significantly soften the polyimide matrix (Figure 1b). To synthesize the block copolymer, PLA with a number-average molecular weight (M_n) of 50 kDa was first synthesized via a ring-opening polymerization using 3-(Boc-amino)-1-propanol as the initiator and DBU as the catalyst (Figures 2a and S1). The deprotection of the *tert*-butoxycarbonyl (Boc) end group generated amine-terminated PLA (PLA-NH_2) (Figure S2). Then, PLA-NH_2 was reacted with PMDA and oDA to produce a polylactide-*b*-poly(amic acid)-*b*-polylactide (PLA-*b*-PAA-*b*-PLA) triblock copolymer. We targeted a PLA weight fraction (ϕ_{PLA}) of 40% to access the bicontinuous phase of the triblock copolymer so that the final polyimide film would contain interconnected mesopores.[67] The actual ϕ_{PLA} was determined based on ^{1}H NMR (Figure 2a). Peak *b* corresponded to the methine protons in PLA repeating units and Peak *c* to all aromatic protons in poly(amic acid) repeating units (Figure 2a). The integral ratio of Peak *c* and Peak *b*, I_b:I_c = 39.0:100, indicated an actual ϕ_{PLA} of 40.2% using eq 1.

$$\phi_{PLA} = \frac{I_b \times M_{PLA}}{I_b \times M_{PLA} + I_c/10 \times M_{PAA}} \quad (1)$$

where I_b, I_c are the integrals of Peak *b* and *c*, respectively. M_{PLA} = 72.1 g/mol and M_{PAA} = 418 g/mol are the molar masses of PLA and poly(amic acid) repeating units, respectively.

PLA-*b*-PAA-*b*-PLA triblock copolymers, mixed with acetic anhydride and pyridine, were cast into a thin film using DMSO as the solvent. Acetic anhydride and pyridine chemically imidized poly(amic acid) into polyimide, ensuring the film with high thermal and structural stabilities and to survive the subsequent thermolysis.[68] Removing PLA without perturbing the polyimide matrix necessitated a low thermolysis temperature. Thermogravimetric analysis of polylactide-*b*-polyimide-*b*-polylactide (PLA-*b*-PI-*b*-PLA) thin films showed three weight-loss regimes (Figure 2b). The initial weight loss below 260 °C arose from the evaporation of volatile species, such as the solvent and chemical imidization reagents. The weight loss between 260 and 440 °C was assigned to the thermal decomposition of PLA.[69] The remaining weight evolving from 89.4 to 54.5% indicated a ϕ_{PLA} of 39.0% in the dry PLA-*b*-PI-*b*-PLA film, concurring with the ϕ_{PLA} calculated using ^{1}H NMR (Figure 2a). The weight loss above 440 °C was due to the decomposition of polyimide matrices.[70] To remove the PLA phase without plasticizing the polyimide matrix, 280 °C was selected as the thermolysis temperature to prepare mesoporous polyimide thin films. To confirm that thermolysis at 280 °C could slowly remove the PLA phase, we used isothermal gravimetric analysis to monitor the weight loss of PLA-*b*-PI-*b*-PLA for 24 h (Figure 2c). The PLA decomposition in the first hour resulted in a weight loss of 8.3%. In the subsequent hours, the incremental weight loss per hour decreased gradually. The cumulative weight loss approached 37.5% after 24 h, implying the removal of most of the PLA phase.

https://doi.org/10.1021/acsnano.3c04159
ACS Nano 2024, 18, 155−163

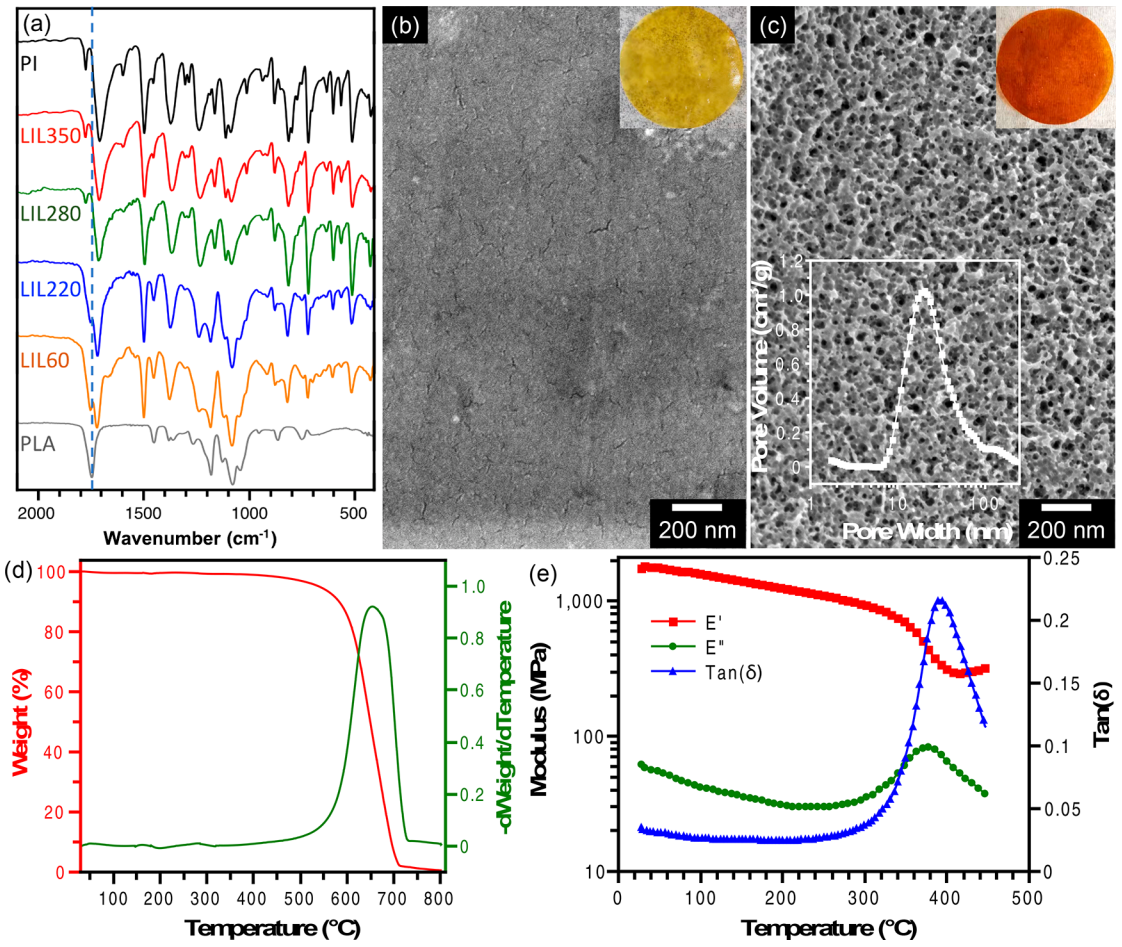

Figure 3. Thermolysis and microstructures of mesoporous polyimide films. (a) FT-IR spectra of PLA, PI, and PLA-*b*-PI-*b*-PLA (LIL) thermalized at 60, 220, 280, and 350 °C. The dashed line at 1752 cm^{-1} corresponds to the carbonyl stretching of PLA. (b) Before and (c) after thermolysis at 280 °C for 24 h, PLA-*b*-PI-*b*-PLA thin films show a nonporous and mesoporous morphology, respectively. The insets show the optical images of 19 mm wide PLA-*b*-PI-*b*-PLA discs. The pore size distribution of the mesoporous polyimide film indicates a median pore width of 21 nm. (d) Thermogravimetric analysis of the mesoporous polyimide thin film shows a $T_{d,5\%}$ of 540 °C. (e) Dynamic mechanical analysis shows a high storage modulus E' of 1.80 GPa at RT. The E' is greater than E'' at all temperatures between 25 and 450 °C.

The evolution of the PLA content and the degree of imidization were recorded using ATR FT-IR employing the PLA-NH_2 and commercial PMDA-oDA polyimides as references (Figure 3a). The efficient chemical imidization of PLA-*b*-PI-*b*-PLA was confirmed by the profound peaks at 1777, 1717, and 1370 cm^{-1}, corresponding to the asymmetric stretching of C=O, symmetric stretching of C=O, and stretching of C−N in polyimides, respectively.[71−73] The peak at 1752 cm^{-1} was assigned to the C=O stretching of PLA.[74−76] The PLA-*b*-PI-*b*-PLA thin film heating at 220 °C for 24 h retained strong PLA C=O stretching. After thermolysis at 280 °C for 24 h, the absence of C=O stretching at 1752 cm^{-1} indicated the removal of PLA. PMDA-oDA polyimide usually requires a high temperature for complete imidization. After heating at 350 °C for 1 h, the appearance of PLA-*b*-PI-*b*-PLA resembled that of commercial polyimide, confirming a high degree of imidization. The morphologies of PLA-*b*-PI-*b*-PLA before and after thermolysis were imaged using SEM, confirming the mesopore development (Figures 3b,c and S3). The as-cast PLA-*b*-PI-*b*-PLA thin film showed a nonporous flat surface. After thermolysis, interconnected mesopores formed in the polyimide matrices. The color of PLA-*b*-PI-*b*-PLA films changed from amber to brownish due to the formation of charge-transfer complexes in polyimides.[77] Nitrogen sorption analysis suggested that the mesopores had a median size of 21 nm (Figures 3c inset and S4).

The mesoporous polyimide separators must have high thermal stability and mechanical strength to ensure electrode segregation both under working conditions and during the thermal runaway.[78] Thermogravimetric analysis confirmed the excellent thermal stability of mesoporous polyimide films, showing a $T_{d,5\%}$ of 540 °C (Figure 3d). PLA was completely removed, as evidenced by no additional weight loss related to PLA. The thermomechanical properties of mesoporous polyimide were further tested using dynamic mechanical analysis (DMA). The mesoporous polyimide film exhibited a storage modulus (E') of ∼1.80 GPa at room temperature and retained an E' of 0.94 GPa at 300 °C (Figure. 3e). E' was greater than E'' in the tested temperature range, affording a maximum of tan(δ) at 393 °C and confirming the high thermomechanical stability. The high modulus of mesoporous polyimide separators would cease the dendritic growth and enable the safe cycling of lithium−metal batteries.[1,63]

As a benchmark, the electrochemical performance of mesoporous polyimide was evaluated along with commercial PP/PE/PP separators. The electrochemical impedance of both

https://doi.org/10.1021/acsnano.3c04159
ACS Nano 2024, 18, 155−163

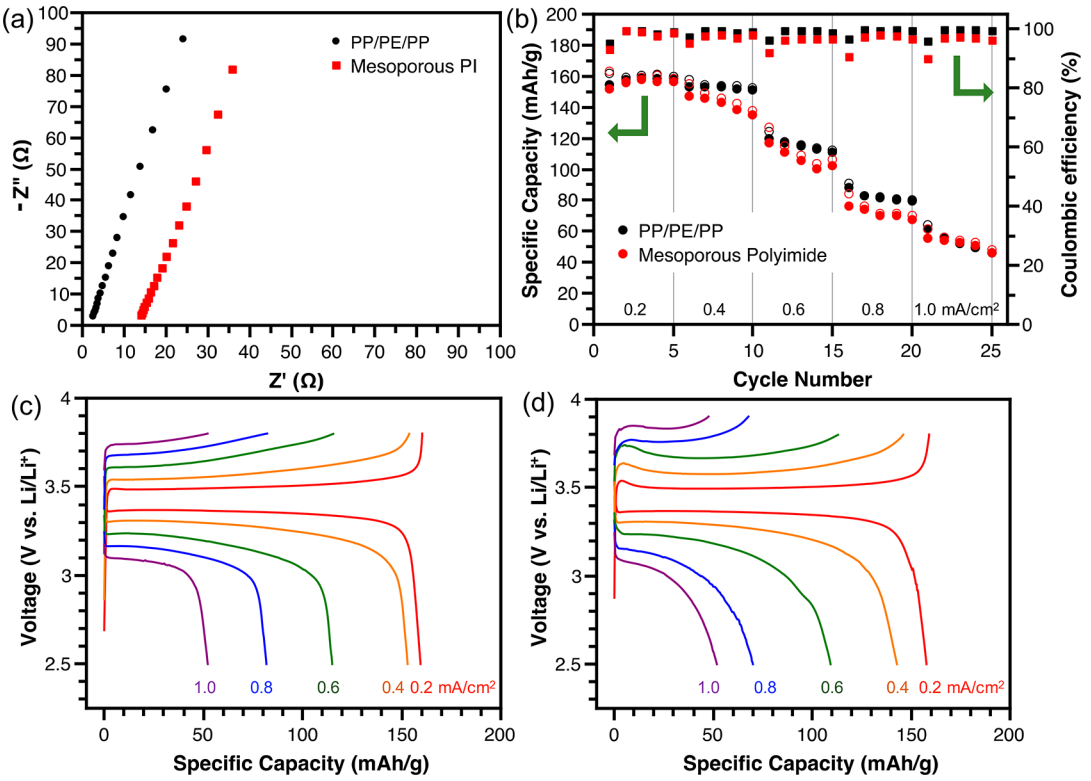

Figure 4. Electrochemical performance of mesoporous polyimide separators. (a) The ionic impedances, (b) rate capabilities, and (c,d) voltage profiles of (c) PP/PE/PP and (d) mesoporous polyimide separators are compared. Current densities ranging from 0.2 to 1.0 mA/cm^2 were employed in (b–d). Mesoporous polyimide separators show comparable good performance with PP/PE/PP separators. Cathode: $LiFePO_4$ on aluminum foil (12 mg/cm^2, 12 mm in diameter).

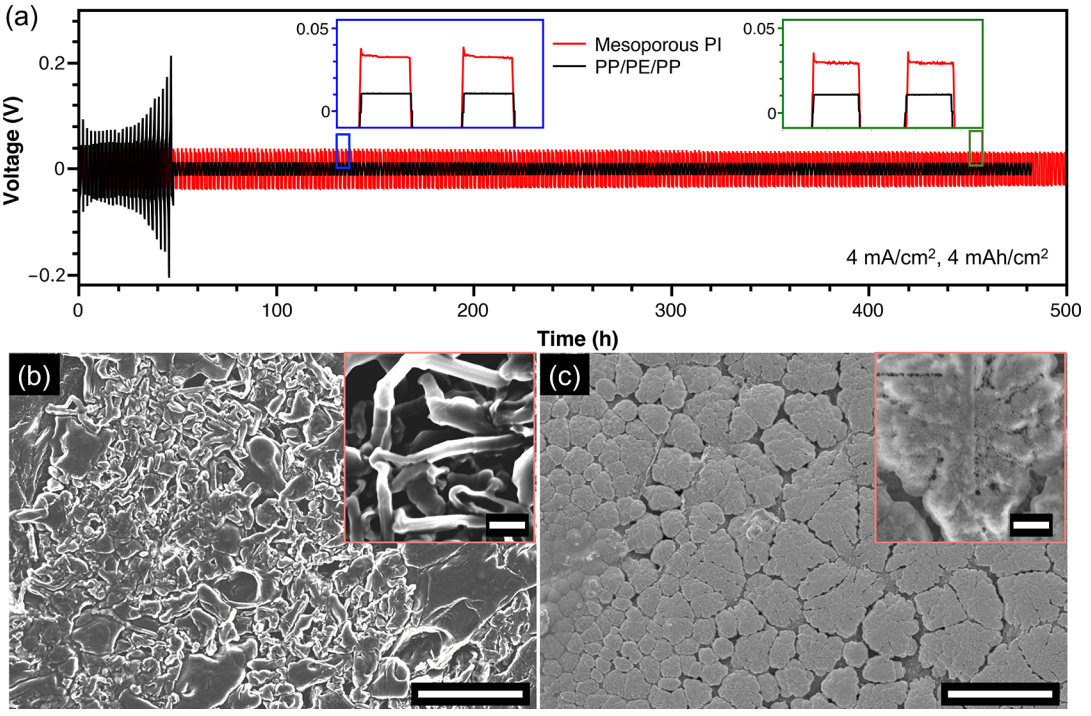

Figure 5. Li/Li symmetric battery test. (a) The voltage profile indicates the battery employing a PP/PE/PP separator encounters a short circuit after 50 h of cycling, whereas the mesoporous polyimide separator enables safe charging/discharging without short circuits for 500 h. The insets show the detailed voltage profiles after cycling for 130 and 450 h. (b) After charging/discharging for 130 h, the lithium–metal electrode contacting a PP/PE/PP separator shows a dendritic morphology. The zoomed-in view shows kinked dendrites with a width of 200 nm. (c) The lithium–metal electrode contacting a mesoporous polyimide separator shows flat-top protrusions. The zoomed-in view shows the detailed morphology of a lithium protrusion. Scale bars in both (b) and (c), 5 μm. In zoomed-in views, 500 nm.

https://doi.org/10.1021/acsnano.3c04159
ACS Nano 2024, 18, 155–163

separators was measured between two stainless steel spacers (Figure 4a). The impedances were 2.6 Ω for PP/PE/PP and 13 Ω for the mesoporous polyimide. The smaller pore size caused a higher impedance of mesoporous polyimide separators. It thus hindered ion transport, which could be tuned by the block copolymer molecular weight and volume fraction as well as the separator thickness. Both separators were tested in $LiFePO_4$/lithium coin cells at increasing current densities from 0.2 to 1.0 mA/cm^2. The mesoporous polyimide separator showed rate capabilities comparable to those of the PP/PE/PP separator (Figure 4b). Despite a higher ionic impedance than the PP/PE/PP separator, the mesoporous polyimide separator exhibited a slightly higher initial overpotential, e.g., 3.76 vs 3.70 V at a current density of 0.8 mA/cm^2 (Figure 4c,d).

The dendrite-suppressing capability of mesoporous polyimide separators was tested in symmetric Li/Li batteries at a current density of 4 mA/cm^2 and a capacity of 4 mAh/cm^2 (Figures 5a and S5). The symmetric Li/Li battery employing the PP/PE/PP separator showed a growing overpotential after 30 h, corresponding to the increasing internal impedance due to the dendritic growth, electrolyte consumption, and thick SEI formation. After 57 h, the lithium dendrites penetrated the PP/PE/PP separator and caused an internal short circuit, resulting in an abrupt decrease of potential to 0.01 V. In contrast, the mesoporous polyimide separator effectively suppressed the lithium dendrites and retained a stable potential for >500 h.

The morphologies of lithium−metal electrodes in both batteries were imaged by using SEM after charging/discharging for 130 h (Figure 5b,c). With the PP/PE/PP separator in the battery, sharp lithium dendrites grew on the lithium−metal electrode, and an average dendrite width was 200 nm (Figure 5b). Since the pore sizes in the PP/PE/PP separator were 40−400 nm,[33] the lithium dendrites traversed the large pores and caused short circuits. In contrast, in the battery with a mesoporous polyimide separator, flat-top lithium protrusions formed on the electrode, absent of any sharp lithium dendrites (Figure 5c).

The mesoporous polyimide separators show outstanding dendrite-suppressing capability because of three characteristics: (i) the mesopores allow uniform Li^+ flux across the separator, minimizing the dendritic growth;[61,62] (ii) the mesopore width is smaller than the width of lithium dendrites, preventing dendrites from penetrating the separator; (iii) the high modulus withstands the high axial stress, ceasing the invasion of lithium dendrites.[1,63−66] The smaller pore size, however, slows ion transport, resulting in a slightly higher overpotential. Reducing the ionic impedance will be an important aspect of future optimizations. Decreasing the thickness of mesoporous polyimide separators and shortening the ion diffusion length will be attractive means to reduce the apparent ionic impedance.

CONCLUSION

In this contribution, a mesoporous polyimide thin film was produced via slow thermolysis of a polylactide-*b*-polyimide-*b*-polylactide triblock copolymer. The slow thermolysis at 280 °C gradually removed polylactide to create mesopores of 21 nm without perturbing the polyimide matrix. The resulting mesoporous polyimide thin films exhibited a storage modulus of 1.80 GPa. The mesoporous structures and high modulus together contributed to an excellent dendrite-suppressing capability. Separated by mesoporous polyimide, lithium only formed flat-top protrusions, enabling safe cycling for >500 h. This work highlights the potential of uniform mesoporous engineering polymers for dendrite suppression. We anticipate the mesoporous polyimide separators to be applicable to suppressing dendrites in "beyond Li-ion" energy storage technologies.

EXPERIMENTAL SECTION

Chemicals. D,L-Lactide was recrystallized in ethyl acetate before use as follows. D,L-Lactide (10.0 g, Sigma-Aldrich) was dissolved in ethyl acetate (15.0 mL, Fisher Scientific) at 75 °C and stored at −4 °C for 1 h. Afterward, pure white lactide crystals were collected via vacuum filtration and dried overnight at reduced pressure. 3-(Boc-amino)-1-propanol (Sigma-Aldrich) was heated at 120 °C under reduced pressure for 2 h to remove moisture and then stored over 4 Å molecular sieves. Chloroform (Fisher Scientific) was stirred with CaH_2 (Sigma-Aldrich) overnight and distilled before use. 1,8-Diazabicyclo[5.4.0]undec-7-ene (DBU), dichloromethane (DCM), trifluoroacetic acid (TFA), sodium bicarbonate, anhydrous dimethyl sulfoxide (DMSO), pyromellitic dianhydride (PMDA), 4,4′-oxidianiline (oDA), benzoyl chloride, acetic anhydride, pyridine, and ninhydrin were purchased from Sigma-Aldrich and used as received. Deuterated chloroform ($CDCl_3$) and DMSO (DMSO-d_6) were purchased from Cambridge Isotope Laboratories. $LiPF_6$ in EC/DEC (1 M, Sigma-Aldrich) was utilized as the liquid electrolyte. In battery tests, $LiFePO_4$ coated on aluminum foil (120 g/m^2, 68 μm coating thickness, MTI Corp.) was employed as the cathode and lithium foil (0.20 mm thickness, Signa-Aldrich) as the anode. Battery cases, spacers, and springs (MTI Corporation) were cleaned via sonication in a mixture of acetone/isopropanol (v:v = 1:1) for 1 h and dried at 80 °C overnight. The polypropylene/polyethylene/polypropylene trilayer separators (PP/PE/PP, Celgard 2325) were purchased from Celgard, LLC.

Instrumentation. Proton nuclear magnetic resonance (^{1}H NMR) spectra were collected in $CDCl_3$ or DMSO-d_6 on a 400 MHz Varian Unity. Thermal gravimetric analysis (TGA) was conducted on a TGA 5500 (TA Instruments) in the air. Fourier transform infrared spectroscopy (FT-IR) was performed on a Thermo Scientific Nicolet iS5 spectrometer with an iD7 ATR accessory. Nitrogen adsorption was performed on a Micromeritics 3Flex Adsorption Analyzer. Scanning electron microscopy (SEM) was conducted on an LEO Zeiss 1550. Dynamic mechanical analysis (DMA) was performed on a TA Q800. Oxygen plasma etching was conducted in a South Bay Technology PC-2000 using a forward power of 60 W. The coin cells were crimped on an MTI MSK-160 E. Electrochemical impedance spectroscopy (EIS) was performed on a PARSTAT 4000, Princeton Applied Research-AMETEK. The lithium−metal batteries and lithium/lithium batteries were tested on a Neware BTS4000.

Polymerization of Boc-Terminated Polylactide (Boc-PLA). To a 100 mL Schlenk tube, D,L-lactide (8.50 g) and 3-(Boc-amino)-1-propanol (18.3 mg) were dissolved in anhydrous chloroform (60.0 mL). The resulting solution was degassed in three freeze−pump−thaw cycles. Afterward, DBU (15.9 mg) was added to the solution in an argon-filled glovebox. The resulting solution was stirred at room temperature for 1 h. The polymerization was terminated by adding benzoyl chloride (30.0 mg) and stirring the mixture for another 1.5 h. Subsequently, the solution was poured into a chilled methanol (300.0 mL). The white precipitates were collected as the product via vacuum filtration and then dried at 80 °C overnight *in vacuo*.

Synthesis of Amine-Terminated Polylactide (PLA-NH_2). Boc-PLA (4.00 g) was dissolved in a mixture of DCM and TFA (v:v = 1:1, 40.0 mL in total) and reacted overnight. Afterward, the solvents were removed on a rotary evaporator. The resulting viscous residue was dissolved in DCM (50.0 mL) and then neutralized using a saturated $NaHCO_3$ aqueous solution. The organic phase was collected and poured into chilled methanol (300 mL). The PLA-NH_2 product as white precipitates was collected by using vacuum filtration and dried at 70 °C overnight *in vacuo*.

https://doi.org/10.1021/acsnano.3c04159
ACS Nano 2024, 18, 155−163

Synthesis of Polylactide-*b*-poly(amic acid)-*b*-polylactide (PLA-*b*-PAA-*b*-PLA) Triblock Copolymer. In a 500 mL round-bottom flask, PLA-NH_2 (3.022 g), PMDA (2.588 g), and oDA (2.370 g) were dissolved in anhydrous DMSO (150.0 mL). The mixture was stirred at room temperature for 12 h and then heated at 100 °C for another 12 h.

Preparation of Mesoporous Polyimide Films. An aliquot of PLA-*b*-PAA-*b*-PLA in DMSO solution (5.0 mL) was mixed with acetic anhydride (220 μL) and pyridine (70 μL) and then poured onto a glass slide (7.0 × 7.0 cm). The solution layer was baked at 60 °C under reduced pressure to produce a thin film. The film was further baked stepwise at 100 °C for 1 h, 150 °C for 1 h, 220 °C for 1 h, 280 °C for 24 h, and 350 °C for 1 h. The resulting thin film was peeled off from the supporting glass slide, and then, both sides were etched using oxygen plasma for 30 min to enhance the wettability of the liquid electrolytes. The plasma-activated mesoporous polyimide film showed fast and almost complete wetting by the electrolyte, superior to the wettability of PP/PE/PP separator with a contact angle of 43−47°.[79,80] The final porous polyimide thin film of 17.4 μm thickness was cut into discs of 19 mm in diameter and used as a battery separators.

Battery Assembly and Tests. The mesoporous polyimide separators were tested in CR2032 coin cells by using electrochemical impedance spectroscopy (EIS), lithium−metal half batteries and lithium/lithium symmetric batteries. For EIS batteries, the separators were interposed between two stainless steel spacers filled with 30 μL of electrolyte. The EIS batteries were conditioned at room temperature for 24 h before testing. The potentiostatic EIS measurement was carried out over a frequency range of 10^5 to 1 Hz at an amplitude of 5 mV. Eight data points were collected per decade of frequency. For lithium−metal batteries, $LiFePO_4$ on aluminum foil (12 mm in diameter, 12 mg/cm^2) and lithium foil (15 mm in diameter) were employed as the cathodes and anodes, respectively. The volume of electrolyte was 60 μL. For lithium/lithium symmetric batteries, separators were inserted between two lithium−metal electrodes filled with 60 μL of electrolyte. The PP/PE/PP separators have a thickness of 18.3 ± 0.8 μm and a pore size of 40−400 nm (Figure S6a),[33] whereas the mesoporous polyimide separators have a thickness of 17.4 ± 1.7 μm and a pore width of 21 nm. (Figure S6b,c).

ASSOCIATED CONTENT

Supporting Information

The Supporting Information is available free of charge at https://pubs.acs.org/doi/10.1021/acsnano.3c04159.

Kinetics of the ring-opening polymerization of lactide using a DBU catalyst. Ninhydrin tests of amine-terminated PLA. Morphologies of LIL films on the top, cross-section, and bottom surface before and after the thermolysis. Pore size analysis of mesoporous polyimide thin films. Initial voltage profile of Li/Li symmetric cells comprising PP/PE/PP and mesoporous polyimide separators. Cross-sectional images of PP/PE/PP and mesoporous polyimide separators (PDF)

AUTHOR INFORMATION

Corresponding Author

Guoliang Liu − *Department of Chemistry, Macromolecules Innovation Institute, and Division of Nanoscience, Academy of Integrated Science, Virginia Tech, Blacksburg, Virginia 24061, United States;* orcid.org/0000-0002-6778-0625; Email: gliu1@vt.edu

Authors

Dong Guo − *Department of Chemistry, Virginia Tech, Blacksburg, Virginia 24061, United States;* orcid.org/0000-0002-3469-2602

Linqin Mu − *Department of Chemistry, Virginia Tech, Blacksburg, Virginia 24061, United States;* orcid.org/0000-0003-4421-4820

Feng Lin − *Department of Chemistry, Virginia Tech, Blacksburg, Virginia 24061, United States;* orcid.org/0000-0002-3729-3148

Complete contact information is available at: https://pubs.acs.org/10.1021/acsnano.3c04159

Author Contributions

D.G. and L.M. performed early experimental explorations on the electrochemical performance. D.G. conducted the experiments. D.G., F.L., and G.L. designed the experiments. D.G. and G.L. wrote the paper. G.L. conceived the project and participated in all the data interpretations. All authors agreed to submit the final manuscript.

Funding

This material is based upon work supported by the National Science Foundation under Grant No. DMR-1752611 and the American Chemical Society Petroleum Research Foundation Doctoral New Investigator Award.

Notes

The authors declare the following competing financial interest(s): The authors have filed a patent based on this work.

ACKNOWLEDGMENTS

The authors acknowledge the use of facilities in Nanoscale Characterization and Fabrication Laboratory (NCFL) at the Institute for Critical Technology and Applied Science (ICTAS), Virginia Tech.

REFERENCES

(1) He, Y.; Ren, X.; Xu, Y.; Engelhard, M. H.; Li, X.; Xiao, J.; Liu, J.; Zhang, J. G.; Xu, W.; Wang, C. Origin of Lithium Whisker Formation and Growth under Stress. *Nat. Nanotechnol.* **2019**, *14*, 1042−1047.

(2) Cao, X.; Ren, X.; Zou, L.; Engelhard, M. H.; Huang, W.; Wang, H.; Matthews, B. E.; Lee, H.; Niu, C.; Arey, B. W.; Cui, Y.; Wang, C.; Xiao, J.; Liu, J.; Xu, W.; Zhang, J.-G. Monolithic Solid−Electrolyte Interphases Formed in Fluorinated Orthoformate-Based Electrolytes Minimize Li Depletion and Pulverization. *Nat. Energy* **2019**, *4*, 796−805.

(3) Tarascon, J. M.; Armand, M. Issues and Challenges Facing Rechargeable Lithium Batteries. *Nature* **2001**, *414*, 359−367.

(4) Li, L.; Basu, S.; Wang, Y.; Chen, Z.; Hundekar, P.; Wang, B.; Shi, J.; Shi, Y.; Narayanan, S.; Koratkar, N. Self-Heating-Induced Healing of Lihtium Dendrites. *Science* **2018**, *359*, 1513−1516.

(5) Mukhopadhyay, A.; Jangid, M. K. Li Metal Battery, Heal Thyself. *Science* **2018**, *359*, 1463.

(6) Lin, D.; Liu, Y.; Cui, Y. Reviving the Lithium Metal Anode for High-Energy Batteries. *Nat. Nanotechnol.* **2017**, *12*, 194−206.

(7) Frenck, L.; Sethi, G. K.; Maslyn, J. A.; Balsara, N. P. Factors That Control the Formation of Dendrites and Other Morphologies on Lithium Metal Anodes. *Front. Energy Res.* **2019**, *7*, 115.

(8) Bieker, G.; Winter, M.; Bieker, P. Electrochemical in Situ Investigations of SEI and Dendrite Formation on the Lithium Metal Anode. *Phys. Chem. Chem. Phys.* **2015**, *17*, 8670−8679.

(9) Niu, C.; Pan, H.; Xu, W.; Xiao, J.; Zhang, J. G.; Luo, L.; Wang, C.; Mei, D.; Meng, J.; Wang, X.; Liu, Z.; Mai, L.; Liu, J. Self-Smoothing Anode for Achieving High-Energy Lithium Metal Batteries under Realistic Conditions. *Nat. Nanotechnol.* **2019**, *14*, 594−601.

(10) Bai, P.; Li, J.; Brushett, F. R.; Bazant, M. Z. Transition of Lithium Growth Mechanisms in Liquid Electrolytes. *Energy Environ. Sci.* **2016**, *9*, 3221−3229.

(11) Deng, Q.; Hu, R.; Xu, C.; Chen, B.; Zhou, J. Modeling Fracture of Solid Electrolyte Interphase in Lithium-Ion Batteries During Cycling. *J. Solid State Electrochem.* **2019**, *23*, 2999−3008.
(12) Peled, E.; Menkin, S. Review—SEI: Past, Present and Future. *J. Electrochem. Soc.* **2017**, *164*, A1703−A1719.
(13) Shi, F.; Pei, A.; Boyle, D. T.; Xie, J.; Yu, X.; Zhang, X.; Cui, Y. Lithium Metal Stripping beneath the Solid Electrolyte Interphase. *Proc. Natl. Acad. Sci. U.S.A.* **2018**, *115*, 8529−8534.
(14) Gireaud, L.; Grugeon, S.; Laruelle, S.; Yrieix, B.; Tarascon, J. M. Lithium Metal Stripping/Plating Mechanisms Studies: A Metallurgical Approach. *Electrochem. Commun.* **2006**, *8*, 1639−1649.
(15) Liu, Z.; Zinkevich, T.; Indris, S.; He, X.; Liu, J.; Xu, W.; Bai, J.; Xiong, S.; Mo, Y.; Chen, H. $Li_{15}P_4S_{16}Cl_3$, a Lithium Chlorothiophosphate as a Solid-State Ionic Conductor. *Inorg. Chem.* **2020**, *59*, 226−234.
(16) Chen, R.; Li, Q.; Yu, X.; Chen, L.; Li, H. Approaching Practically Accessible Solid-State Batteries: Stability Issues Related to Solid Electrolytes and Interfaces. *Chem. Rev.* **2020**, *120*, 6820−6877.
(17) Ji, X.; Hou, S.; Wang, P.; He, X.; Piao, N.; Chen, J.; Fan, X.; Wang, C. Solid-State Electrolyte Design for Lithium Dendrite Suppression. *Adv. Mater.* **2020**, *32*, 2002741.
(18) Ansari, Y.; Guo, B.; Cho, J. H.; Park, K.; Song, J.; Ellison, C. J.; Goodenough, J. B. Low-Cost, Dendrite-Blocking Polymer-Sb_2O_3 Separators for Lithium and Sodium Batteries. *J. Electrochem. Soc.* **2014**, *161*, A1655−A1661.
(19) Liang, J.; Chen, Q.; Liao, X.; Yao, P.; Zhu, B.; Lv, G.; Wang, X.; Chen, X.; Zhu, J. A Nano-Shield Design for Separators to Resist Dendrite Formation in Lithium-Metal Batteries. *Angew. Chem., Int. Ed.* **2020**, *59*, 6561−6566.
(20) Chen, S.; Zheng, J.; Mei, D.; Han, K. S.; Engelhard, M. H.; Zhao, W.; Xu, W.; Liu, J.; Zhang, J. G. High-Voltage Lithium-Metal Batteries Enabled by Localized High-Concentration Electrolytes. *Adv. Mater.* **2018**, *30*, 1706102.
(21) Li, Q.; Tan, S.; Li, L.; Lu, Y.; He, Y. Understanding the Molecular Mechanism of Pulse Current Charging for Stable Lithium-Metal Batteries. *Sci. Adv.* **2017**, *3*, 1701246.
(22) Maeyoshi, Y.; Ding, D.; Kubota, M.; Ueda, H.; Abe, K.; Kanamura, K.; Abe, H. Long-Term Stable Lithium Metal Anode in Highly Concentrated Sulfolane-Based Electrolytes with Ultrafine Porous Polyimide Separator. *ACS Appl. Mater. Interfaces* **2019**, *11*, 25833−25843.
(23) Wang, J.; Huang, W.; Pei, A.; Li, Y.; Shi, F.; Yu, X.; Cui, Y. Improving Cyclability of Li Metal Batteries at Elevated Temperatures and Its Origin Revealed by Cryo-Electron Microscopy. *Nat. Energy* **2019**, *4*, 664−670.
(24) Cao, D.; Xing, Y.; Tantratian, K.; Wang, X.; Ma, Y.; Mukhopadhyay, A.; Cheng, Z.; Zhang, Q.; Jiao, Y.; Chen, L.; Zhu, H. 3D Printed High-Performance Lithium Metal Microbatteries Enabled by Nanocellulose. *Adv. Mater.* **2019**, *31*, 1807313.
(25) Xie, J.; Wang, J.; Lee, H. R.; Yan, K.; Li, Y.; Shi, F.; Huang, W.; Pei, A.; Chen, G.; Subbaraman, R.; Christensen, J.; Cui, Y. Engineering Stable Interfaces for Three-Dimensional Lithium Metal Anodes. *Sci. Adv.* **2018**, *4*, eaat5168.
(26) Zhao, C.-Z.; Chen, P.-Y.; Zhang, R.; Chen, X.; Li, B.-Q.; Zhang, X.-Q.; Cheng, X.-B.; Zhang, Q. An Ion Redistributor for Dendrite-Free Lithium Metal Anodes. *Sci. Adv.* **2018**, *4*, eaat3446.
(27) Fang, C.; Lu, B.; Pawar, G.; Zhang, M.; Cheng, D.; Chen, S.; Ceja, M.; Doux, J.-M.; Musrock, H.; Cai, M.; Liaw, B.; Meng, Y. S. Pressure-Tailored Lithium Deposition and Dissolution in Lithium Metal Batteries. *Nat. Energy* **2021**, *6*, 987−994.
(28) Guo, J.; Wen, Z.; Wu, M.; Jin, J.; Liu, Y. Vinylene Carbonate−$LiNO_3$: A Hybrid Additive in Carbonic Ester Electrolytes for SEI Modification on Li Metal Anode. *Electrochem. Commun.* **2015**, *51*, 59−63.
(29) Varzi, A.; Raccichini, R.; Passerini, S.; Scrosati, B. Challenges and Prospects of the Role of Solid Electrolytes in the Revitalization of Lithium Metal Batteries. *J. Mater. Chem. A* **2016**, *4*, 17251−17259.
(30) Zhao, Q.; Liu, X.; Stalin, S.; Khan, K.; Archer, L. A. Solid-State Polymer Electrolytes with in-Built Fast Interfacial Transport for Secondary Lithium Batteries. *Nat. Energy* **2019**, *4*, 365−373.
(31) Zhao, W.; Yi, J.; He, P.; Zhou, H. Solid-State Electrolytes for Lithium-Ion Batteries: Fundamentals, Challenges and Perspectives. *EER* **2019**, *2*, 574−605.
(32) Horstmann, B.; Shi, J.; Amine, R.; Werres, M.; He, X.; Jia, H.; Hausen, F.; Cekic-Laskovic, I.; Wiemers-Meyer, S.; Lopez, J.; Galvez-Aranda, D.; Baakes, F.; Bresser, D.; Su, C.-C.; Xu, Y.; Xu, W.; Jakes, P.; Eichel, R.-A.; Figgemeier, E.; Krewer, U.; Seminario, J. M.; Balbuena, P. B.; Wang, C.; Passerini, S.; Shao-Horn, Y.; Winter, M.; Amine, K.; Kostecki, R.; Latz, A. Strategies Towards Enabling Lithium Metal in Batteries: Interphases and Electrodes. *Energy Environ. Sci.* **2021**, *14*, 5289−5314.
(33) Peter, C.; Nikolowski, K.; Reuber, S.; Wolter, M.; Michaelis, A. Chronoamperometry as an Electrochemical in Situ Approach to Investigate the Electrolyte Wetting Process of Lithium-Ion Cells. *J. Appl. Electrochem.* **2020**, *50*, 295−309.
(34) Shimizu, Y.; Kanamura, K. Effect of Pore Size in Three Dimensionally Ordered Macroporous Polyimide Separator on Lithium Deposition/Dissolution Behavior. *J. Electrochem. Soc.* **2019**, *166*, A754−A761.
(35) Wang, H.; Wang, T.; Yang, S.; Fan, L. Preparation of Thermal Stable Porous Polyimide Membranes by Phase Inversion Process for Lithium-Ion Battery. *Polymer* **2013**, *54*, 6339−6348.
(36) Lin, C.-E.; Zhang, H.; Song, Y.-Z.; Zhang, Y.; Yuan, J.-J.; Zhu, B.-K. Carboxylated Polyimide Separator with Excellent Lithium Ion Transport Properties for a High-Power Density Lithium-Ion Battery. *J. Mater. Chem. A* **2018**, *6*, 991−998.
(37) Lin, D.; Zhuo, D.; Liu, Y.; Cui, Y. All-Integrated Bifunctional Separator for Li Dendrite Detection via Novel Solution Synthesis of a Thermostable Polyimide Separator. *J. Am. Chem. Soc.* **2016**, *138*, 11044−11050.
(38) Jiang, W.; Liu, Z.; Kong, Q.; Yao, J.; Zhang, C.; Han, P.; Cui, G. A High Temperature Operating Nanofibrous Polyimide Separator in Li-Ion Battery. *Solid State Ion.* **2013**, *232*, 44−48.
(39) Lee, J.; Lee, C.-L.; Park, K.; Kim, I.-D. Synthesis of an Al_2O_3-Coated Polyimide Nanofiber Mat and Its Electrochemical Characteristics as a Separator for Lithium Ion Batteries. *J. Power Sources* **2014**, *248*, 1211−1217.
(40) Zhou, Z.; Zhao, T.; Lu, X.; Cao, H.; Zha, X.; Zhou, Z. Functionalized Polyimide Separators Enable High Performance Lithium Sulfur Batteries at Elevated Temperature. *J. Power Sources* **2018**, *396*, 542−550.
(41) Wang, L.; Deng, N.; Fan, L.; Wang, L.; Wang, G.; Kang, W.; Cheng, B. A Novel Hot-Pressed Electrospun Polyimide Separator for Lithium-Sulfur Batteries. *Mater. Lett.* **2018**, *233*, 224−227.
(42) Pai, J. Y.; Ku, H. Y.; Lin, C. C.; Chiang, C. W.; Hardwick, L. J.; Hu, C. C. Porous Polyimide Separator Promotes Uniform Lithium Plating for Lithium-Free Cells. *Electrochem. Sci. Adv.* **2022**, *2*, e2100091.
(43) Miyata, S.; Yoshida, K.; Shirokura, H.; Kashio, M.; Nagai, K. Solid and Thermal Properties of ABA-Type Triblock Copolymers Designed Using Difunctional Fluorine-Containing Polyimide Macroinitiators with Methyl Methacrylate. *Polym. Int.* **2009**, *58*, 1148−1159.
(44) Fu, G. D.; Zong, B. Y.; Kang, E. T.; Neoh, K. G.; Lin, C. C.; Liaw, D. J. Nanoporous Low-Dielectric Constant Polyimdie Films via Poly(Amic Acid)s with RAFT-Graft Copolymerized Methyl Methacrylate Side Chains. *Ind. Eng. Chem. Res.* **2004**, *43*, 6723−6730.
(45) Hedrick, J. L.; Hawker, C. J.; DiPietro, R.; Jérôme, R.; Charlier, Y. The Use of Styrenic Copolymers to Generate Polyimide Nanofoams. *Polymer* **1995**, *36*, 4855−4866.
(46) Guo, D.; Khan, A. U.; Liu, T.; Zhou, Z.; Liu, G. Sub-10 nm Domains in High-Performance Polyetherimides. *Polym. Chem.* **2019**, *10*, 379−385.
(47) Hedrick, J. L.; DiPietro, R.; Plummer, C. J. G.; Hilborn, J.; Jérôme, R. Polyimide Foams Derived from a High T_g Polyimide with Grafted Poly(α-Methylstyrene). *Polymer* **1996**, *37*, 5229−5236.

https://doi.org/10.1021/acsnano.3c04159
ACS Nano 2024, 18, 155−163

(48) Charlier, Y.; Hedrick, J. L.; Russell, T. P.; Swanson, S.; Sanchez, M.; Jérôme, R. Crosslinked Polyimide Foams Derived from Pyromellitic Dianhydride and 1,1-Bis(4-Aminophenyl)-1-Phenyl-2,2,3-Trifluoroethane with Poly(α-Methylstyrene). *Polymer* **1995**, *36*, 1315−1320.
(49) Hedrick, J. L.; Russell, T. P.; Sanchez, M.; DiPietro, R.; Swanson, S.; Mecerreyes, D.; Jerome, R. Polyimide Nanofoams from Caprolactone-Based Copolymers. *Macromolecules* **1996**, *29*, 3642−3646.
(50) Ju, J.; Wang, Q.; Wang, T.; Wang, C. Low Dielectric, Nanoporous Fluorinated Polyimide Films Prepared from PCL-PI-PCL Triblock Copolymer Using Retro-Diels-Alder Reaction. *J. Colloid Interface Sci.* **2013**, *404*, 36−41.
(51) Meleshko, T. K.; Kashina, A. V.; Saprykina, N. N.; Kostyuk, S. V.; Vasilenko, I. V.; Nikishev, P. A.; Yakimanskii, A. V. Synthesis and Morphology of Polycaprolactone−Block-Polyimide−Block-Polycaprolactone Triblock Copolymers for Film Separation Membranes. *Russ. J. Appl. Chem.* **2017**, *90*, 602−612.
(52) Liu, C.; Liu, B.; Chan-Park, M. B. Synthesis of Polycaprolactone-Polyimide-Polycaprolactone Triblock Copolymers via a 2-Step Sequential Copolymerization and Their Application as Carbon Nanotube Dispersants. *Polym. Chem.* **2017**, *8*, 674−681.
(53) Wang, L.; Lu, J.; Liu, M.; Lin, L.; Li, J. Preparation of Porous Polyimide Microspheres by Thermal Degradation of Block Copolymers. *Particuology* **2014**, *14*, 63−70.
(54) Hedrick, J. L.; Carter, K.; Sanchez, M.; Di Pietro, R.; Swanson, S.; Jayaraman, S.; McGrath, J. G. Crosslinked Polyimide Foams Derived from Poly(Imide-Propylene Oxide) Copolymers. *Macromol. Chem. Phys.* **1997**, *198*, 549−559.
(55) Hedrick, J. L.; Russell, T. P.; Labadie, J.; Lucas, M.; Swanson, S. High Temperature Nanofoams Derived from Rigid and Semi-Rigid Polyimides. *Polymer* **1995**, *36*, 2685−2697.
(56) Chung, C.-M.; Lee, J.-H.; Cho, S.-Y.; Kim, J.-G.; Moon, S.-Y. Preparation of Porous Thin Films of a Partially Aliphatic Polyimide. *J. Appl. Polym. Sci.* **2006**, *101*, 532−538.
(57) Charlier, Y.; Hedrick, J.; Russell, T. P.; Jonas, A.; Volksen, W. High Temperature Polymer Nanofoams Based on Amorphous, High T_g Polyimides. *Polymer* **1995**, *36*, 987−1002.
(58) Carter, K. R.; DiPietro, R. A.; Sanchez, M. I.; Swanson, S. A. Nanoporous Polyimides Derived from Highly Fluorinated Polyimide/Poly(Propylene Oxide) Copolymers. *Chem. Mater.* **2001**, *13*, 213−221.
(59) Cannarella, J.; Liu, X.; Leng, C. Z.; Sinko, P. D.; Gor, G. Y.; Arnold, C. B. Mechanical Properties of a Battery Separator under Compression and Tension. *J. Electrochem. Soc.* **2014**, *161*, F3117−F3122.
(60) Kalnaus, S.; Wang, Y.; Turner, J. A. Mechanical Behavior and Failure Mechanisms of Li-Ion Battery Separators. *J. Power Sources* **2017**, *348*, 255−263.
(61) Chen, X. R.; Yao, Y. X.; Yan, C.; Zhang, R.; Cheng, X. B.; Zhang, Q. A Diffusion−Reaction Competition Mechanism to Tailor Lithium Deposition for Lithium-Metal Batteries. *Angew. .Chem. Int. Ed.* **2020**, *59*, 7743−7747.
(62) Nagasaki, M.; Kanamura, K. High-Performance Lithium Metal Rechargeable Battery Using an Ultrafine Porous Polyimide Separator with Three-Dimensionally Ordered Macroporous Structure. *ACS Appl. Energy Mater.* **2019**, *2*, 3896−3903.
(63) Ferrese, A.; Newman, J. Mechanical Deformation of a Lithium-Metal Anode Due to a Very Stiff Separator. *J. Electrochem. Soc.* **2014**, *161*, A1350−A1359.
(64) Monroe, C.; Newman, J. The Impact of Elastic Deformation on Deposition Kinetics at Lithium/Polymer Interfaces. *J. Electrochem. Soc.* **2005**, *152*, A396−A404.
(65) Na, W.; Lee, A. S.; Lee, J. H.; Hwang, S. S.; Kim, E.; Hong, S. M.; Koo, C. M. Lithium Dendrite Suppression with UV-Curable Polysilsesquioxane Separator Binders. *ACS Appl. Mater. Interfaces* **2016**, *8*, 12852−12858.
(66) Wan, J.; Xie, J.; Kong, X.; Liu, Z.; Liu, K.; Shi, F.; Pei, A.; Chen, H.; Chen, W.; Chen, J.; Zhang, X.; Zong, L.; Wang, J.; Chen, L. Q.; Qin, J.; Cui, Y. Ultrathin, Flexible, Solid Polymer Composite Electrolyte Enabled with Aligned Nanoporous Host for Lithium Batteries. *Nat. Nanotechnol.* **2019**, *14*, 705−711.
(67) Guo, D.; Riet, J.; Khan, A.; Guo, Y.; Xu, Z.; Liu, T.; Liu, G. Mesoporous Polyetherimide Thin Films via Hydrolysis of Polylactide-*b*-Polyetherimide-*b*-Polylactide. *Polym. Chem.* **2021**, *12*, 3939−3946.
(68) Yu, H.-C.; Jung, J.-W.; Choi, J.-Y.; Chung, C.-M. Kinetic Study of Low-Temperature Imidization of Poly(Amic Acid)s and Preparation of Colorless, Transparent Polyimide Films. *J. Polym. Sci., Part A: Polym. Chem.* **2016**, *54*, 1593−1602.
(69) Ohkita, T.; Lee, S.-H. Thermal Degradation and Biodegradability of Poly (Lactic Acid)/Corn Starch Biocomposites. *J. Appl. Polym. Sci.* **2006**, *100*, 3009−3017.
(70) Zaragoza, S.; Álvarez, A.; Álvarez, B.; López-Beceiro, J.; Naya, S.; Forcén, P.; Artiaga, R. Thermogravimetric Study of Thermal Degradation of Polyetherimide. *J. Appl. Polym. Sci.* **2015**, *132*, 42329.
(71) Lee, S.-C.; Tai, F.-C.; Wei, C.-H.; Yu, J.-I. ATR-FTIR and Nanoindentation Measurements of PMDA-ODA Polyimide Film under Different Curing Temperature. *Mater. Trans.* **2007**, *48*, 1554−1557.
(72) Wang, C.; Cao, S.; Chen, W.; Xu, C.; Zhao, X.; Li, J.; Ren, Q. Synthesis and Properties of Fluorinated Polyimides with Multi-Bulky Pendant Groups. *RSC Adv.* **2017**, *7*, 26420−26427.
(73) Grabiec, E.; Schab-Balcerzak, E.; Wolińska-Grabczyk, A.; Jankowski, A.; Jarząbek, B.; Kożuch-Krawczyk, J.; Kurcok, M. Physical, Optical and Gas Transport Properties of New Processable Polyimides and Poly(Amideimide)s Obtained from 4,4′-[Oxybis(4,1-Phenylenethio)]Dianiline and Aromatic Dianhydrides. *Polym. J.* **2011**, *43*, 621−629.
(74) Savaris, M.; Braga, G. L.; dos Santos, V.; Carvalho, G. A.; Falavigna, A.; Machado, D. C.; Viezzer, C.; Brandalise, R. N. Biocompatibility Assessment of Poly(Lactic Acid) Films after Sterilization with Ethylene Oxide in Histological Study in Vivo with Wistar Rats and Cellular Adhesion of Fibroblasts in Vitro. *Int. J. Polym. Sci.* **2017**, *2017*, 1−9.
(75) Cuiffo, M. A.; Snyder, J.; Elliott, A. M.; Romero, N.; Kannan, S.; Halada, G. P. Impact of the Fused Deposition (FDM) Printing Process on Polylactic Acid (PLA) Chemistry and Structure. *Appl. Sci.* **2017**, *7*, 579.
(76) Tang, G.; Huang, X.; Ding, H.; Wang, X.; Jiang, S.; Zhou, K.; Wang, B.; Yang, W.; Hu, Y. Combustion Properties and Thermal Degradation Behaviors of Biobased Polylactide Composites Filled with Calcium Hypophosphite. *RSC Adv.* **2014**, *4*, 8985−8993.
(77) Lee, T.-H.; Kim, J. H.; Bae, B.-S. Synthesis of Colorless Imide Hybrid Nanocomposites Using Amine Functionalized Oligosiloxane Nano-Building Clusters. *J. Mater. Chem.* **2006**, *16*, 1657−1664.
(78) Zhu, Y.; Xie, J.; Pei, A.; Liu, B.; Wu, Y.; Lin, D.; Li, J.; Wang, H.; Chen, H.; Xu, J.; Yang, A.; Wu, C.-L.; Wang, H.; Chen, W.; Cui, Y. Fast Lithium Growth and Short Circuit Induced by Localized-Temperature Hotspots in Lithium Batteries. *Nat. Commun.* **2019**, *10*, 2067.
(79) Parikh, D.; Christensen, T.; Hsieh, C.-T.; Li, J. Elucidation of Separator Effect on Energy Density of Li-Ion Batteries. *J. Electrochem. Soc.* **2019**, *166*, A3377−A3383.
(80) Sun, G.; Guo, J.; Niu, H.; Chen, N.; Zhang, M.; Tian, G.; Qi, S.; Wu, D. The Design of a Multifunctional Separator Regulating the Lithium Ion Flux for Advanced Lithium-Ion Batteries. *RSC Adv.* **2019**, *9*, 40084−40091.

https://doi.org/10.1021/acsnano.3c04159
ACS Nano 2024, 18, 155−163